Research Square

Preprints are preliminary reports that have not undergone peer review.
They should not be considered conclusive, used to inform clinical practice,
or referenced by the media as validated information.

High-spatiotemporal-resolution stress and acoustic emission monitoring across the brittle–plastic transition in olivine under true triaxial compression

Rikuto Honda

honda.rikuto.2r@kyoto-u.ac.jp

Kyoto University: Kyoto Daigaku https://orcid.org/0009-0000-5925-2112

Tomoaki Kubo

Kyushu University: Kyushu Daigaku

Noriyoshi Tsujino

Japan Synchrotron Radiation Research Institute: Koeki Zaidan Hojin Kokido Hikari Kagaku Kenkyu Center

Yuji Higo

Japan Synchrotron Radiation Research Institute: Koeki Zaidan Hojin Kokido Hikari Kagaku Kenkyu Center

Sho Kakizawa

Japan Synchrotron Radiation Research Institute: Koeki Zaidan Hojin Kokido Hikari Kagaku Kenkyu Center

Yuta Goto

Kyushu University: Kyushu Daigaku

Sanae Koizumi

National Institute for Materials Science: Busshitsu Zairyo Kenkyu Kiko

Tomohiro Ohuchi

Ehime Daigaku

Hirokatsu Yumoto

Japan Synchrotron Radiation Research Institute: Koeki Zaidan Hojin Kokido Hikari Kagaku Kenkyu Center

Takahisa Koyama

Japan Synchrotron Radiation Research Institute: Koeki Zaidan Hojin Kokido Hikari Kagaku Kenkyu Center

Hiroshi Yamazaki

Japan Synchrotron Radiation Research Institute: Koeki Zaidan Hojin Kokido Hikari Kagaku Kenkyu Center

Yasunori Senba

Japan Synchrotron Radiation Research Institute: Koeki Zaidan Hojin Kokido Hikari Kagaku Kenkyu Center

Haruhiko Ohashi
Japan Synchrotron Radiation Research Institute: Koeki Zaidan Hojin Kokido Hikari Kagaku Kenkyu Center

Ichiro Inoue
RIKEN: Rikagaku Kenkyujo

Yujiro Hayashi
RIKEN: Rikagaku Kenkyujo

Makina Yabashi
RIKEN: Rikagaku Kenkyujo

Research Article

Keywords: brittle-plastic transition, in-situ X-ray observation, acoustic emission, stress mapping

Posted Date: November 25th, 2026

DOI: https://doi.org/10.21203/rs.3.rs-11479232/v1

License: This work is licensed under a Creative Commons Attribution 4.0 International License.
Read Full License

High-spatiotemporal-resolution stress and acoustic emission monitoring across the brittle–plastic transition in olivine under true triaxial compression

Rikuto Honda[a*†], Tomoaki Kubo[b], Noriyoshi Tsujino[c], Yuji Higo[c], Sho Kakizawa[c], Yuta Goto[a], Sanae Koizumi[d,e], Tomohiro Ohuchi[f], Hirokatsu Yumoto[c,g], Takahisa Koyama[c,g], Hiroshi Yamazaki[c,g], Yasunori Senba[c,g], Haruhiko Ohashi[c,g], Ichiro Inoue[g], Yujiro Hayashi[g], Makina Yabashi[g]

[a] Department of Earth and Planetary Sciences, Graduate School of Sciences, Kyushu University, Fukuoka 819-0395, Japan

[b] Department of Earth and Planetary Sciences, Faculty of Sciences, Kyushu University, Fukuoka 819-0395, Japan

[c] Japan Synchrotron Radiation Research Institute, 1-1-1 Kouto, Sayo-cho, Sayo-gun, Hyogo 679-5198, Japan

[d] National Institute for Materials Science, 1-2-1 Sengen, Tsukuba, Ibaraki 305-0047, Japan.

[e] Earthquake Research Institute, The University of Tokyo, 1-1-1 Yayoi, Bunkyo-ku, Tokyo 113-0032, Japan

[f] Geodynamics Research Center, Ehime University, 2-5 Bunkyo-cho, Matsuyama, Ehime 790-8577, Japan

[g] RIKEN SPring-8 Center, 1-1-1 Kouto, Sayo-cho, Sayo-gun, Hyogo 679-5148, Japan.

[†]present address: Institute for Geothermal Sciences, Graduate School of Science, Kyoto University, Beppu, Oita 874-0903, Japan.

[*]Corresponding author: honda.rikuto.2r@kyoto-u.ac.jp

Abstract

Understanding fault formation around the brittle–plastic transition requires experimental measurements that can resolve rapid changes in deformation mode and stress during faulting. Synchrotron radiation provides a powerful method for probing these processes in situ under high-pressure conditions, but the spatiotemporal resolution available with conventional bending-magnet sources has been insufficient to capture the evolution of faulting. In this study, we developed a high-spatiotemporal-resolution measurement technique using a high-flux 100 keV pink beam at SPring-8 and applied it to olivine under true triaxial cold-compression at pressures up to 5 GPa using a multi-anvil type apparatus. Combined with acoustic emission (AE) measurements, this approach allowed us to resolve rapid and spatially heterogeneous deformation processes across the brittle–plastic transition. We successfully detected stress drops accompanied by AEs occurring within 0.3–0.6 s, while the failure stress and fault geometry suggested an influence of the intermediate principal stress. We also resolved spatial stress heterogeneity associated with brittle and semi-brittle fracturing, followed by stress homogenization during plastic deformation. These results demonstrate the potential of this approach for investigating rapid and spatially heterogeneous deformation processes under high-pressure conditions, providing a new experimental basis for understanding faulting processes across the brittle–plastic transition relevant to subduction-zone seismicity.

Keywords: brittle-plastic transition, in-situ X-ray observation, acoustic emission, stress mapping

1. Introduction

Rock deformation in subduction zones shifts from brittle faulting to plastic flow with increasing pressure and temperature through the brittle–plastic transition (BPT). The BPT is particularly important because it marks a fundamental change from localized, potentially unstable faulting to distributed plastic deformation. Although numerous experimental studies have investigated frictional behavior in the brittle regime and flow laws in the plastic regime, deformation processes across the BPT, especially in the semi-brittle regime, remain poorly understood.

Previous frictional experiments have often focused on crustal rocks and sediments (e.g., Blanpied et al. 1995; Chen et al. 2020; Okuda et al. 2023), whereas relatively few studies have investigated olivine, the principal mineral of the mantle wedge and the subducting slab. Most frictional experiments on olivine have been conducted by using gas-medium apparatuses at pressures up to 300 MPa, constraining the temperature dependence of its frictional behavior at relatively low pressures (Boettcher et al. 2007; King and Marone 2012). However, frictional and deformation behavior also strongly depend on pressure, highlighting the need to investigate the mechanical behavior of olivine over a broad pressure range extending into the gigapascal BPT

regime.

Understanding fault formation processes across the BPT requires characterization of not only macroscopic mechanical properties such as frictional behavior, but also local mechanical heterogeneities such as stress concentrations at asperities. Beginning with direct optical observations of frictional contacts (Dieterich and Kilgore 1994), laboratory fault experiments have revealed heterogeneous stress distributions along fault surfaces and their relationships with slip nucleation and rupture propagation (e.g., Selvadurai and Glaser 2017; Pozzi et al. 2025). However, how such fault-scale stress heterogeneity evolves at GPa pressures, particularly across the BPT where the dominant deformation behavior changes markedly, remains largely unexplored.

Another important factor in understanding fault formation across the BPT is the effect of the intermediate principal stress (σ_2). Previous experiments have demonstrated that rock failure depends not only on the maximum and minimum principal stresses (σ_1 and σ_3) but also on σ_2 (e.g., Wiebols and Cook 1968; Mogi 1971; Colmenares and Zoback 2002; Haimson and Rudnicki 2010). However, most deformation experiments have been conducted under conventional triaxial compression under a confining pressure ($\sigma_1>\sigma_2=\sigma_3$), and true triaxial compression ($\sigma_1>\sigma_2>\sigma_3$) has rarely been explored under high-pressure conditions.

Investigating these processes requires experimental techniques that enable deformation at GPa pressures while resolving rapid stress changes and spatial stress heterogeneity, and monitoring

78 acoustic emissions (AEs) associated with fracturing. Multi-anvil type deformation apparatuses
79 provide a powerful platform for controlled deformation experiments under such conditions and
80 can be combined with multiple AE transducers to determine the timing and hypocenter locations
81 of fracture events (e.g., Schubnel et al. 2013; Ohuchi et al. 2022; Matsuda et al. 2026; Honda et
82 al. 2026). Recent studies combining in situ X-ray measurements with AE monitoring have begun
83 to resolve stress drops during deformation and establish their temporal relationship with AE
84 activity (Honda et al. 2026). However, conventional measurements using bending-magnet (BM)
85 radiation sources have typically had temporal resolutions on the order of 10^2 s, making it difficult
86 to resolve rapid processes such as abrupt stress drops during fault slip. This limitation has recently
87 been overcome by the development of high-energy, high-flux pink beams from insertion device
88 (ID) radiation sources and focusing optics with multilayer mirrors (Koyama et al. 2024; Yumoto
89 et al. 2025), enabling sub-second stress measurements during deformation in multi-anvil
90 apparatuses (Ohuchi et al. 2026). These advances now make it possible to explore both rapid
91 stress changes and their spatial heterogeneity across the BPT.
92 In this study, we combine high-spatiotemporal-resolution stress measurements with multi-
93 point AE measurements to investigate the mechanical behavior of olivine across the BPT during
94 cold compression at pressures up to 5 GPa. In addition to the sub-second stress measurements,
95 spatial scanning of the incident beam enables stress mapping across the sample to characterize

96 the distribution and evolution of local stress heterogeneity. We also developed a modified
97 experimental cell geometry to generate true triaxial compression and assess the effect of the
98 intermediate principal stress on the mechanical behavior across the BPT. Using these
99 complementary measurements, we evaluate how deformation mechanisms, local stress
100 heterogeneity, and AE activity evolve with pressure across the transition from brittle faulting to
101 plastic flow in olivine.
102
103 **2. Methods**
104 We conducted a true triaxial cold compression experiment by using DIA-type apparatus
105 "Hyakushiki" installed at BL05XU (currently at BL15XU) of SPring-8 (Fig. S1a). MA 6-6 system
106 (Nishiyama et al. 2008) was employed, which consisted of second stage anvils with a truncation
107 edge length of 6 mm and a cubic pressure medium (9 mm on a side) made from a powder mixture
108 of boron and epoxy in a mass ratio of 4:1. The starting material was a cylindrical synthetic
109 polycrystal of forsterite (grain size of several μm; Koizumi et al. 2010) with a diameter of 1.4 mm
110 and a height of 2.0 mm. It was enclosed in a lifebuoy-shaped capsule, in which two types of
111 cylinders were alternately arranged dividing them into four segments (Fig. 1). In the X-ray
112 incident direction, same sintered boron-epoxy mixture as the pressure medium was used, and
113 processed NaCl pellets were placed on the opposite side (Fig. 1b). Au foils (10 μm thick) were

114 placed above and below the assembly as strain markers and it was sandwiched between alumina
115 pistons. This design was expected to create a true triaxial condition during the cold compression,
116 such that the principal stress axes of the sample ($\sigma_1 > \sigma_2 > \sigma_3$) were approximately aligned with σ_1
117 in the vertical direction, σ_2 along the X-ray, and σ_3 perpendicular to both.
118 Compression proceeded at a constant loading rate of 10 kN min^{-1} up to a maximum load of
119 300 kN (confining pressure of 4.6 GPa). During the experiments, we performed X-ray in situ
120 observations using a 100 keV pink beam at BL05XU (Yumoto et al. 2025). Two-dimensional X-
121 ray diffraction patterns (2D-XRD; Fig. 2) were continuously collected from the center of the
122 sample every 0.3–0.5 s during compression and automatically recorded using a flat-panel detector
123 (Rad-icon1520, Teledyne). Radiographic images were also acquired at the beginning and end of
124 the experiment using a CMOS camera.
125 A rotating slit system developed in Ohsumi et al. (2026) was used to control the incident X-
126 ray beam (Fig. S1b). The system consists of two disks equipped with slits of different widths (200
127 μm and 2 mm) arranged at 45° intervals and the X-ray beam passes through the overlapping
128 portions of the slits. Rotation of the disks enables automatic switching between the two slit widths,
129 while the exposure time can be controlled by adjusting the rotation speed. A trigger signal is
130 generated upon switching the slit width, allowing synchronized operation of the flat panel detector,
131 CMOS camera and the press stage.

Using this function to synchronize XRD acquisition with movement of the precision press stage, we also performed stress mapping at 50 kN intervals during compression. At each interval, compression was paused and the stage was moved in 200 μm steps, with an exposure time of 0.5 s at each position. The measurement was initiated from the uppermost part of the sample within the region observable through the anvil gap and continued until diffraction peaks from the sample were no longer detected. Each mapping measurement consisted of 40–63 steps and required 160–220 s.

Stress and confining pressure were determined from the azimuthal variations in lattice spacing and unit-cell volume, respectively, obtained from the 2D-XRD patterns. The patterns were divided into 60 segments along the azimuthal direction to obtain one-dimensional X-ray diffraction profiles, and at least three of the forsterite reflections (021, 101, 130, 131, and 112) were used for analysis. Stress was determined by fitting the azimuthal variations in lattice spacing to the strain equation (Singh 1993; Singh et al. 1998) (Fig. 3), using elastic constants and their pressure and temperature dependences (Isaak 1992; Abramson et al. 1997). The uncertainty in the determined stress was up to ±0.1 GPa. Similarly, by fitting the volume data, we derived the hydrostatic unit-cell volume and estimated the confining pressure from the equation of state of forsterite (Katsura et al. 2009).

The strain of the sample was determined from the ratio of the sample length before and after

150 compression, with a correction for isotropic volumetric compression. Specifically, the initial (l_0)
151 and final (l) sample length and the volumetric change $\Delta V/V_0$ were used to calculate the strain as
152 $\varepsilon=-\ln(l/l_0)+\Delta V/3V_0$. The average strain rate was then estimated by dividing the strain by the total
153 compression time, excluding the holding periods. This approach provides an estimate of the bulk
154 strain accumulated during compression, rather than its temporal evolution, because the limited
155 optical field of view (~1 mm) covered only a small portion of the sample, preventing continuous
156 measurement of its length during the experiment.

157 The AE measurements were also conducted simultaneously to monitor the stability of
158 deformation. The basic system is the same as that used in our previous studies and detailed
159 information is provided elsewhere (Iwasato et al. 2020; Kubo et al. 2025). We employed the lead
160 zirconate-titanate piezoelectric ceramics (FUJICERA C-6; 0.3 mm thickness and 3 mm diameter)
161 as transducers and attached them to the back of each second stage anvils. They were connected to
162 the amplifiers (20 dB) with coaxial cables, and AE signals were recorded with an oscilloscope
163 (MSO58, Tektronix) after being triggered by the threshold voltage of 20 mV. We set the sampling
164 rate, data-point interval, and amplitude resolution to 125 MHz, 8.0 ns, and 0.1 mV (12 bits),
165 respectively. The clocks of the AE recording system and XRD acquisition system were
166 synchronized with an accuracy of ±0.5 s. Using the Lab-VIEW AE analysis system (Iwasato et al.
167 2020), the arrival times of waveforms were automatically picked using the AIC method (Akaike

168 1974) after band-pass filtering within the range of 0.2–15 MHz. A P-wave velocity of 8 km s^{-1}
169 was assumed to determine the hypocenter locations, for which half the sampling interval (±4 ns)
170 corresponds to a propagation distance of ±32 μm. The sum of squared amplitudes was computed,
171 and AE magnitude was defined based on the energy E as $M_{AE} = \log(E/E_0)$. Here, E_0 was taken as
172 the minimum energy previously obtained with this system (2.78 x10^{-10} V^2 s).
173

174 ## 3. Results and discussion

175 *3.1 Sub-second stress evolution and AE activity across the BPT under true triaxial compression*

176 In the brittle regime, the frictional strength of rocks is described by Byerlee's law (Byerlee
177 1978):

178 $$\tau = 0.85\sigma_n \ \ (\sigma_n \leq 200\text{MPa}) \qquad (1a)$$

179 $$\tau = 0.6\sigma_n + 50 \ \ (\sigma_n \geq 200\text{MPa}) \qquad (1b)$$

180 where τ and σ_n are the shear stress and normal stress on a given fault plane, respectively. In triaxial
181 compression experiments, these expressions are often rewritten using differential stress σ and
182 confining pressure P considering the Mohr-Coulomb type failure criterion:

183 $$\sigma = 3.68P \ \ (P \leq 100\text{MPa}) \qquad (2a)$$

184 $$\sigma = 2.12P + 177 \ \ (P \geq 100\text{MPa}) \qquad (2b)$$

185 Thus, the frictional strength in this regime depends solely on pressure and increases linearly with

186 it.

187 Although crack formation is active in the brittle regime, it becomes inhibited with increasing
188 pressure, leading to semi-brittle deformation. The upper-limit of this regime is approximately
189 described by the Goetze criterion ($\sigma = P_c$) (Kohlstedt et al. 1995).

190 At higher pressures and especially at low temperatures, plastic deformation by dislocation
191 glide (i.e., low-temperature plasticity) dominates, exhibiting dependence on strain rate $\dot{\varepsilon}$ and
192 temperature T (Frost and Ashby 1982):

193 $$\dot{\varepsilon} = A\left(\frac{\sigma}{G}\right)^n \exp\left(-\frac{H^*}{RT}\left[1-\left(\frac{\sigma}{\sigma_P}\right)^p\right]^q\right) \quad (3)$$

194 where A, n, p, and q are the constants, G is the shear modulus, H^* is the activation enthalpy, σ_P
195 is the Peierls stress, and R is the gas constant. By comparing the strengths derived from these
196 brittle and plastic deformation laws, we interpreted the mechanical behavior of olivine during
197 cold compression.

198 Fig. 4 shows the evolution of stress in olivine during compression with respect to pressure
199 and load (approximately time). The stress of olivine reached 5.2 GPa at a final pressure of ~4.6
200 GPa and a strain of 44% at 300 kN, with a strain rate of 2.4 x10^{-4} s^{-1}.

201 At the beginning of compression, the stress continued to increase linearly up to 3.4 GPa at a
202 pressure of approximately 1.1 GPa, exceeding the brittle strength given by Byerlee's law. Then
203 the stress suddenly dropped to 1.6 GPa ($\Delta\sigma$ = 1.8 GPa) after which small stress drops ($\Delta\sigma$ = 0.3–

204 0.9 GPa) were repeatedly observed at pressures around 1 GPa (Fig. 5a). During this initial stage
205 of brittle failure, AE events were frequently recorded (24 events/min).

206 With further compression, the stress progressively departed from Byerlee's law as
207 deformation proceeded within the semi-brittle regime. During this stage, the stress initially
208 increased without AE activity, but was followed by another relatively large stress drop ($\Delta\sigma$ = 1.1
209 GPa) accompanied by several AE events at a pressure of 2.1 GPa (Fig. 6a).

210 Beyond this point, at higher pressures, no additional stress drops or AE activity were observed
211 suggesting that deformation was stabilized. In particular, the strength during the final stages of
212 deformation reached a level comparable to the strength of low-temperature plasticity (e.g., Tsenn
213 and Carter 1987; Hansen et al. 2019), indicating that plastic deformation ultimately prevailed.
214 Overall, these observations demonstrate typical BPT behavior: as pressure increases, the stress in
215 olivine progressively departs from the frictional strength and approaches the plastic flow strength,
216 while the frequency of AE events associated with failure and stress drops gradually decreases.

217 The advantage of the sub-second-resolved stress measurements introduced in this study lies
218 in the ability to capture rapid processes that were previously inaccessible in deformation
219 experiments using multi-anvil type apparatuses. Figs. 5a and 6a show magnified views of the
220 intervals around the large stress drops. In the brittle regime (Fig. 5a), the first stress drop occurred
221 at a strength exceeding Byerlee's law and was followed by the repetitive small stress drops on the

222 order of 10^2 MPa slightly below the frictional strength given by Byerlee's law. These stress drops
223 occurred on extremely short time scales of 0.3–0.6 s. This stick-slip behavior was accompanied
224 by intermittent and frequent AE events. The spatial distribution of AE hypocenters in this regime
225 changed markedly during deformation (Fig. 5c). Although AEs were broadly distributed around
226 the piston-sample boundary before the major stress drop (black symbols), they became localized
227 along a distinct plane during stick-slip (blue and red symbols). By fitting a plane to the
228 hypocenters obtained during the stick-slip, the strike of this plane was estimated to be
229 approximately parallel to the σ_2 axis and to have a fault angle of 18° relative to the σ_1 axis (dashed
230 line). In addition, the AE distribution on a plane perpendicular to the strike appears to be locally
231 clustered in a patch-like manner (Fig. 5d).

232 It should be noted that the effect of the intermediate principal stress σ_2 must be considered in
233 the geometry of our experiment. Although it is difficult to determine σ_2 independently with the
234 current methodology, the fact that the first failure event occurred at stresses exceeding Byerlee's
235 law suggests that the maximum strength cannot be explained by simple two-dimensional criteria
236 (Byerlee 1978) and that the influence of σ_2 is indeed present. When friction criteria that
237 incorporate σ_2 are applied, the differential stress at the failure point is generally expected to
238 increase relative to cases in which σ_2 is identical to σ_3 (e.g., Wiebols and Cook 1968; Mogi 1971;
239 Colmenares and Zoback 2002). In addition, there have been experimental reports indicating that

240 σ_2 causes the fault angle relative to σ_1 direction to decrease (e.g., Haimson and Rudnicki 2010).
241 According to the Mohr–Coulomb failure criterion (i.e., Byerlee's law), brittle failure under these
242 conditions is expected to produce a fault angle of ~31° relative to the σ_1 axis, which is larger than
243 that indicated by the AE distribution, suggesting the effect of intermediate principal stress. On the
244 other hand, σ_2 and σ_3 may have been comparable at low confining pressures and differential stress,
245 which likely explains why the low-load data appear to follow Byerlee's law and why the strength
246 during the stick slip did not exceed the frictional strength.

247 In contrast to the brittle regime, AEs occurred only infrequently and were associated with the
248 stress drop within ~0.5 s during deformation in the semi-brittle regime (Fig. 6a). Considering the
249 time resolution of the AE recordings, it is possible that the largest AE occurred slightly before the
250 stress drops. Furthermore, AEs originated from an area different from that in the brittle regime
251 (Figs. 6b–d). These observations suggest contrasting behaviors: in the brittle regime, AE-
252 generating crack formation occurs frequently throughout deformation, whereas in the semi-brittle
253 regime, AEs are observed only around the timing of failure events that induce stress drops.

254 Capturing sub-second phenomena such as stick-slip behavior has been reported in many
255 previous experiments using load cells at low pressure and even on olivine (Boettcher et al. 2007).
256 The methods used in this study greatly improve the time resolution compared with conventional
257 approaches using multi-anvil type apparatus with BM sources (~10^2 s), while still achieving

258 temporal resolution comparable to that of load-cell measurements and enabling direct observation
259 of similar rapid phenomena even at high pressures.
260
261 *3.2 Mapping the evolution of stress heterogeneity across the BPT*
262 Stress mapping conducted at several loads revealed that stress within the sample became more
263 homogeneous as plastic deformation progressively dominated with increasing pressure (Fig. 7).
264 Because the sample was surrounded laterally by the NaCl capsule and bounded above and below
265 by Au foils, relatively low stress values tended to be obtained near the sample boundaries as an
266 experimental artifact. Therefore, pixels near the sample margins were excluded from the
267 quantitative evaluation of stress heterogeneity. It should also be noted that, because diffraction
268 patterns were acquired in transmission through the cylindrical sample, stress variations along the
269 σ_2 direction were spatially averaged.
270 After the step in which many AE events were recorded in the brittle regime (100 kN, 1.8 GPa;
271 Fig. 7a), the mapping showed stress heterogeneity of up to 1.1 GPa, corresponding to 37 % of the
272 average stress. The high-stress region appears to extend obliquely from the lower to the upper
273 part of the sample. This distribution does not necessarily coincide with the AE distribution,
274 suggesting that stuck regions which have not yet undergone slip may appear as high-stress areas.
275 In the semi-brittle regime (150 kN, 2.6 GPa; Fig. 7b), the region that exhibited high stress in

276 the brittle regime continued to sustain relatively high stress, and substantial stress heterogeneity
277 (26%) persisted. In contrast, at higher loads/pressures (300 kN, 4.6 GPa; Fig. 7c), the stress
278 distribution became more uniform, with its heterogeneity decreasing to ~14%, suggesting that
279 plastic deformation prevailed, as seen in the macroscopic mechanical behavior. Thus, spatial
280 mapping of the sample successfully captured both stress heterogeneity associated with fracturing
281 and subsequent stress homogenization, suggesting stabilization of deformation.

282 At relatively low confining pressures, previous laboratory studies have directly visualized
283 heterogeneous stress distributions along frictional interfaces and demonstrated their relationships
284 with asperities and slip instabilities (e.g., Dieterich and Kilgore 1994; Selvadurai and Glaser 2017;
285 Pozzi et al. 2025). In contrast, deformation experiments at GPa pressures approaching the BPT
286 have generally characterized mechanical behavior in terms of bulk stress, providing little
287 information on the spatial distribution of stress associated with fault formation (e.g., Ohuchi et al.
288 2026). The present measurements provide a first step toward bridging this gap by resolving stress
289 heterogeneity during deformation across the BPT at GPa pressures. In the brittle regime, we
290 observed pronounced stress heterogeneity associated with localized deformation, which
291 progressively diminished as deformation became more plastic with increasing pressure.

292 Although the observed stress heterogeneity may reflect local stress concentrations associated
293 with asperity-scale deformation, the present experimental design allows only spatially averaged

stresses to be measured through the cylindrical sample, and the spatial resolution of the mapping is currently limited to a relatively coarse mesh size of 200 μm. In addition, stress mapping with the present system requires several minutes for total acquisition, with the acquisition time increasing with sample size and spatial resolution. Further technical improvements, particularly faster stage scanning, will therefore be required to resolve the rapid stress redistribution associated with unstable slip. Nevertheless, the present measurements demonstrate that spatially resolved stress heterogeneity and its evolution across the BPT can now be characterized under GPa-pressure conditions, extending high-pressure deformation experiments beyond conventional bulk-stress measurements. Although the present study focused on stress measurements, XRD mapping could also be applied to reaction mapping and kinetic analyses, offering additional avenues for future investigation.

4. Conclusion

A true triaxial cold compression experiment was conducted using a multi-anvil type apparatus, with high spatiotemporal resolution observations using a high-flux 100 keV pink beam in combination with AE measurements, to investigate the mechanical behavior associated with the BPT of olivine. We achieved a temporal resolution approximately 10^2 times higher with the ID source than that of conventional in situ experiments using BM sources. This enabled us to

312 successfully capture sub-second stress drops accompanied by AE associated with failure in the
313 brittle to semi-brittle regimes, which had previously been inaccessible. The distribution of AE
314 events suggested that faulting occurred in the brittle regime along a plane with a strike parallel to
315 the intermediate principal stress (σ_2) and a fault angle of ~18° relative to the maximum principal
316 stress (σ_1). This steep fault plane and the strength at the failure point implied the effect of the
317 intermediate principal stress. In the semi-brittle regime, stress drops were observed with fewer
318 AEs, and a large AE was observed at the initiation of faulting.

319 In addition, stress-mapping measurements revealed that stress heterogeneity up to 1.1 GPa
320 existed within the sample in the brittle regime, whereas stress became progressively homogenized
321 as plastic deformation came to dominate. The techniques developed in this study are broadly
322 applicable to the direct experimental investigation of high-pressure phenomena, including
323 visualization of asperities on fault planes and rapid processes such as rock reactions and fracturing.

324

325 **Declarations**

326 **Availability of data and materials**

327 The datasets used and/or analyzed during the current study are available from the corresponding
328 author on reasonable request.

329

Competing interests

The authors declare no competing interests.

Funding

This work was partially supported by JSPS KAKENHI Grant Numbers JP22K18282 and JP24H00274 to T. Kubo, JP23KJ1743 to R. Honda, and JP23H00147 to T. Ohuchi.

Authors' contributions

Conceptualization: R. Honda, T. Kubo. **Formal analysis**: R. Honda. **Investigation**: R. Honda, Y. Goto, T. Kubo. **Resources**: S. Koizumi. **Methodology**: R. Honda, T. Kubo, N. Tsujino, Y. Higo, S. Kakizawa, T. Ohuchi, H. Yumoto, T. Koyama, H. Yamazaki, Y. Senba, H. Ohashi, I. Inoue, Y. Hayashi, M. Yabashi. **Funding acquisition**: R. Honda, T. Kubo, T. Ohuchi. **Writing – original draft**: R. Honda. **Writing – review & editing**: T. Kubo. **Supervision**: T. Kubo.

Acknowledgements

We acknowledge S. Yamanouchi for assistance with experimental preparation. In-situ X-ray observation was conducted at BL05XU of SPring-8 supported by RIKEN (SACLA/SPring-8 Basic Development Program). This study was also supported by ERI JURP 2026-B-08 in

Earthquake Research Institute, the University of Tokyo.

Figure legends

Fig. 1. Cell assembly used in the experiment: (a) side view (σ_2 direction) and (b) top view (σ_1 direction). Black arrows schematically represent the directions of the principal stresses ($\sigma_1 > \sigma_2 > \sigma_3$). Hard alumina pistons were placed above and below the sample. Surrounding the sample, a four-segmented cylinder consisting of two different materials was arranged with boron-epoxy mixture segments parallel to the X-ray beam and NaCl segments perpendicular to it.

Fig. 2. 2D-XRD pattern obtained at ambient pressure. Miller indices (*hkl*) of olivine are assigned to each diffraction peak. Diffraction peaks from the pressure medium are also marked with asterisks (*). The radial and circumferential direction correspond to 2θ and the azimuth angle, respectively.

Fig. 3. Lattice spacing of the olivine 021 plane as a function of azimuthal angle in the brittle (black), semi-brittle (red), and plastic regimes (blue). Pressure and stress conditions are shown in the corresponding colors. Solid lines show fits to the strain equation (Singh 1993; Singh et al. 1998). Arrows indicate the azimuth angles corresponding to maximum and minimum principal

366 stresses.

367

368 **Fig. 4.** Evolution of the average differential stress of olivine (green symbols) and AE magnitude
369 (blue lines; M_{AE}) during cold compression. (a) Stress evolution as a function of pressure. Dark
370 green arrows indicate the stress path, including decreases in pressure associated with stress drop.
371 The black and red lines represent Byerlee's law (Byerlee 1978) and the Goetze criterion
372 (Kohlstedt et al. 1995), respectively, whereas the pink (Tsenn and Carter 1987; TC87) and purple
373 (Hansen et al. 2019; H19) lines indicate the strength for low-temperature plasticity (LTP). (b)
374 Stress as a function of applied load, which approximately represents temporal evolution because
375 of the constant loading rate. Black arrows indicate stress drops. The portions enlarged separately
376 in Fig. 5a and Fig. 6a are indicated as (5a) and (6a), respectively.

377

378 **Fig. 5.** (a) Enlarged view of the stress drops occurring repeatedly at low loads accompanied by
379 intermittent AEs. The error of stress is up to ±0.04 GPa in this range. (b–d) Spatial distribution of
380 AEs obtained in the brittle regime. The hypocenters of AEs recorded within the sample are shown
381 for the intervals from the start of loading to just before the first stress drop (up to 2180 s; black),
382 from the first stress drop to the onset of minor stick–slip events (up to 2202 s; blue), and from the
383 onset to the end of minor stick–slip events (up to 2223 s; red). Gray lines correspond to the

384 estimated sample size from the mapping. The purple dotted line in (c) indicates the intersection
385 between the σ_1–σ_3 plane and the three-dimensional plane (fault plane) fitted to the data shown by
386 the red circles. The black arrow in (d) indicates the cluster of AEs.
387
388 **Fig. 6.** (a) Enlarged view of stress drops observed at intermediate loads. A large AE was detected
389 prior to the drop. The error of stress is up to ±0.06 GPa in this range. (b–d) Spatial distribution of
390 AEs recorded in the semi-brittle regime. The AE observed prior to the stress drop is shown in red.
391 Gray lines correspond to the estimated sample size from the mapping.
392
393 **Fig. 7.** Stress maps obtained at loads (and pressures) of (a) 100 kN (1.8 GPa), (b) 150 kN (2.6
394 GPa), and (c) 300 kN (4.6 GPa). The mesh spacing is 200 μm. The numbers within the white
395 frames indicate the stage positions along the vertical and horizontal axes (in mm). Stress values
396 are shown by the color scales and values within the meshes. Black regions without numbers
397 correspond to areas where sample stress was not measured due to the shadows of the anvils (left
398 side) or the piston region (bottom side). AE hypocenters obtained up to 100 kN and 150 kN are
399 also plotted (color scheme as in Figs. 5 and 6).
400
401 **References**

Abramson E H, Brown J M, Slutsky L J, et al. (1997) The elastic constants of San Carlos olivine to 17 GPa. J. Geophys. Res. 102(6):12253–12263. doi : 10.1029/97JB00682.

Akaike H (1974) A new look at the statistical model identification. IEEE Trans. Autom. Control. 19(6):716-723. doi: 10.1109/TAC.1974.1100705.

Blanpied M L, Lockner D A, Byerlee J D (1995) Frictional slip of granite at hydrothermal conditions. J. Geophys. Res. 100(B7):13045–13064. doi: 10.1029/95JB00862.

Boettcher M S, Hirth G, Evans B (2007) Olivine friction at the base of oceanic seismogenic zones. J. Geophys. Res. 112:B01205. doi: 10.1029/2006JB004301.

Byerlee J (1978) Friction of rocks, Pure Appl. Geophys. 116:615–627. doi: 10.1007/BF00876528.

Chen J, Verberne B A, Niemeijer A R (2020) Flow-to-friction transition in simulated calcite gouge: Experiments and microphysical modeling. J. Geophys. Res. 125: e2020JB019970. doi: 10.1029/2020JB019970.

Colmenares L B, Zoback M D (2002) A statistical evaluation of intact rock failure criteria constrained by polyaxial test data for five different rocks. Int. J. Rock Mech. Min. Sci. 39(6):695–729. doi: 10.1016/S1365-1609(02)00048-5.

Dieterich J H, Kilgore B D (1994) Direct observation of frictional contacts: New insights for state-dependent properties. Pure Appl. Geophys. 143:283–302. doi: 10.1007/BF00874332.

Frost H J, Ashby M F (1982) Deformation-Mechanism Maps: The Plasticity and Creep of Metals

and Ceramics. Oxford: Pergamon Press.

Haimson B, Rudnicki J W (2010) The effect of the intermediate principal stress on fault formation and fault angle in siltstone. J. Struct. Geol. 32(11):1701–1711. doi: 10.1016/j.jsg.2009.08.017.

Hansen L N, Kumamoto K M, Thom C A, et al. (2019) Low-temperature plasticity in olivine: Grain size, strain hardening, and the strength of the lithosphere. J. Geophys. Res. 124:5427–5449. doi: 10.1029/2018JB016736.

Honda R, Kubo T, Miyahara M, et al. (2026) The olivine-ringwoodite transformation triggers deep slab seismicity and rheological weakening. Nat. Commun. 17:5264. doi: 10.1038/s41467-026-71661-z.

Isaak D G (1992) High-temperature elasticity of iron-bearing olivines. J. Geophys. Res. 97(B2):1871–1885. doi: 10.1029/91JB02675.

Iwasato T, Kubo T, Higo Y (2020) Development of MA6-6 type AE monitoring system in D-DIA apparatus. SPring-8/SACLA Research Reports. 8(2):214–218. doi: 10.18957/rr.8.2.214.

Katsura T, Shatskiy A, Manthilake M A G M, et al. (2009) Thermal expansion of forsterite at high pressures determined by in situ X-ray diffraction: The adiabatic geotherm in the upper mantle. Phys. Earth Planet. Inter. 174:86–92. doi: 10.1016/j.pepi.2008.08.002.

King D S H, Marone C (2012) Frictional properties of olivine at high temperature with applications to the strength and dynamics of the oceanic lithosphere. J. Geophys. Res.

117:B12203. doi: 10.1029/2012JB009511.

Kohlstedt D L, Evans B, Mackwell S J (1995) Strength of the lithosphere: Constraints imposed by laboratory experiments. J. Geophys. Res. 100(B9):17587–17602. doi: 10.1029/95JB01460.

Koizumi S, Hiraga T, Tachibana C, et al. (2010) Synthesis of highly dense and fine-grained aggregates of mantle composites by vacuum sintering of nano-sized mineral powders. Phys. Chem. Miner. 37:505–518. doi: 10.1007/s00269-009-0350-y.

Koyama T, Yumoto H, Miura T, et al. (2024) Sub-micrometre focusing of intense 100 keV X-rays with multilayer reflective optics. J. Synchrotron Radiat. 31(2):276–281. doi: 10.1107/S1600577524000213.

Kubo T, Ikehara M, Moriyama K, et al. (2025) Shear deformation experiments up to 10 GPa using the MA6-6 type AE monitoring system. SPring-8/SACLA Research Reports. 13(5):271–277. doi: 10.18957/rr.13.5.271.

Matsuda K, Ohuchi T, Inoue S, et al. (2026) Faulting triggered by a quasi-diffusionless shear transition of olivine in deep subducted slabs. Sci. Adv. 12:eadu5181. doi: 10.1126/sciadv.adu5181

Mogi K (1971) Fracture and flow of rocks under high triaxial compression. J. Geophys. Res. 76(5):1255–1269. doi: 10.1029/JB076i005p01255.

Nishiyama N, Wang Y, Sanehira T, et al. (2008) Development of the multi-anvil assembly 6-6 for

456 DIA and D-DIA type high-pressure apparatus. High Pres. Res. 28:307–314. doi:
457 10.1080/08957950802250607.
458 Ohsumi H, Higo Y, Hayashi Y, et al. (2026) A high-energy X-ray beamline for materials science
459 research at SPring-8: BL15XU. J. Synchrotron Radiat. 33(5):1554-1566. doi:
460 10.1107/S1600577526006387.
461 Ohuchi T, Higo Y, Tange Y, et al. (2022) In situ X-ray and acoustic observations of deep seismic
462 faulting upon phase transitions in olivine. Nat. Commun. 13:5213. doi: 10.1038/s41467-022-
463 32923-8.
464 Ohuchi T, Higo Y, Tsujino N, et al. (2026) Semi-brittle behavior of olivine aggregates revisited.
465 High Pres. Res. 46:187–207. doi: 10.1080/08957959.2026.2639425.
466 Okuda H, Niemeijer A R, Takahashi M, et al. (2023) Hydrothermal friction experiments on
467 simulated basaltic fault gouge and implications for megathrust earthquakes. J. Geophys. Res.
468 128:e2022JB025072. doi: 10.1029/2022JB025072.
469 Pozzi G, Volpe G, Taddeucci J, et al. (2025) Spontaneous complexity in the dynamics of slow
470 laboratory earthquakes. Nat. Commun. 16:8914. doi: 10.1038/s41467-025-63984-0.
471 Schubnel A, Brunet F, Hilairet N, et al. (2013) Deep-focus earthquake analogs recorded at high
472 pressure and temperature in the laboratory. Science. 341(6152):1377–1380. doi:
473 10.1126/science.1240206.

Selvadurai P A, Glaser S D (2017) Asperity generation and its relationship to seismicity on a planar fault: a laboratory simulation. Geophys. J. Int. 208:1009–1025. doi: 10.1093/gji/ggw439.

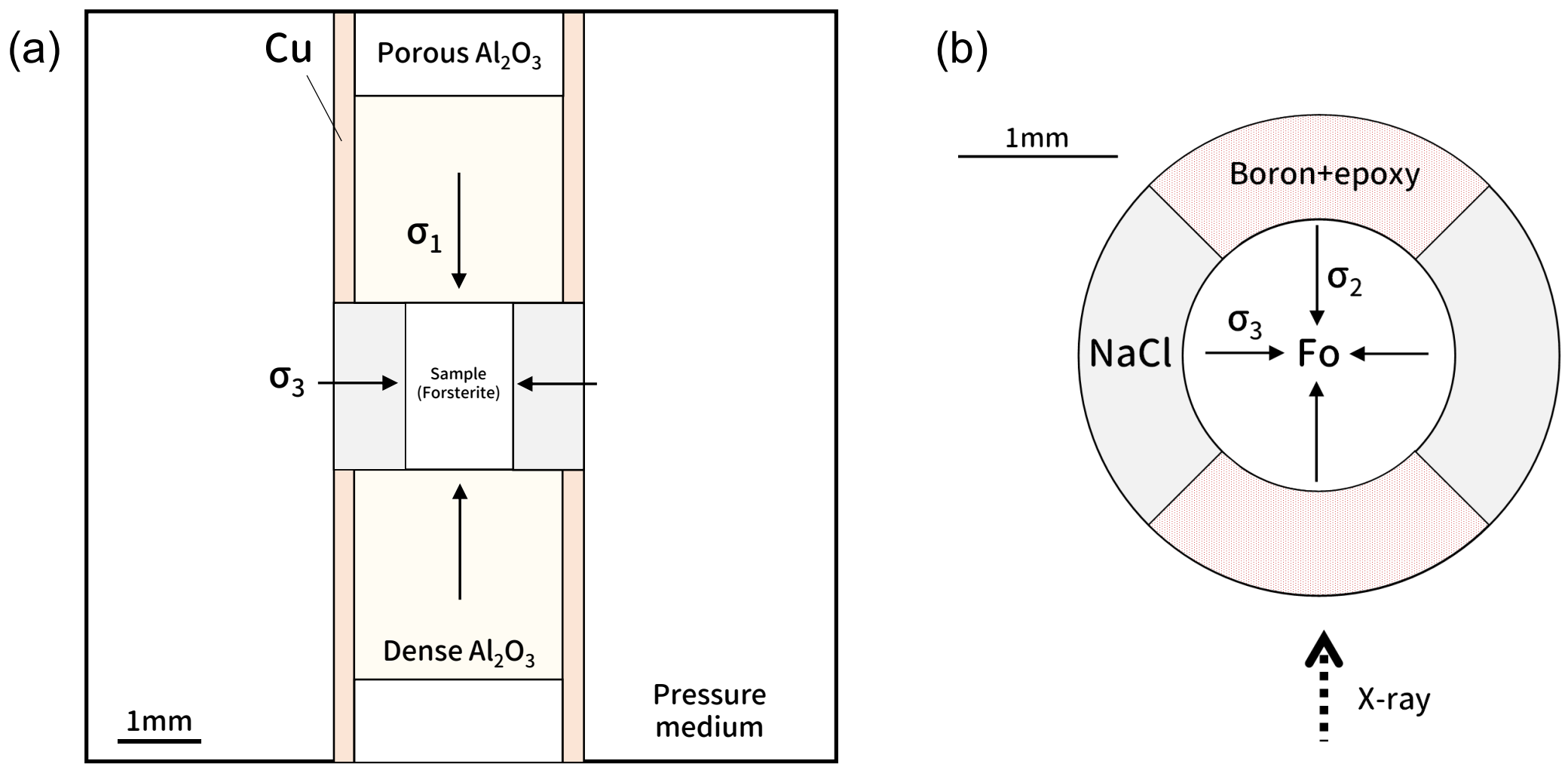
Singh A K (1993) The lattice strains in a specimen (cubic system) compressed nonhydrostatically in an opposed anvil device. J. Appl. Phys. 73(9):4278–4286. doi: 10.1063/1.352809.

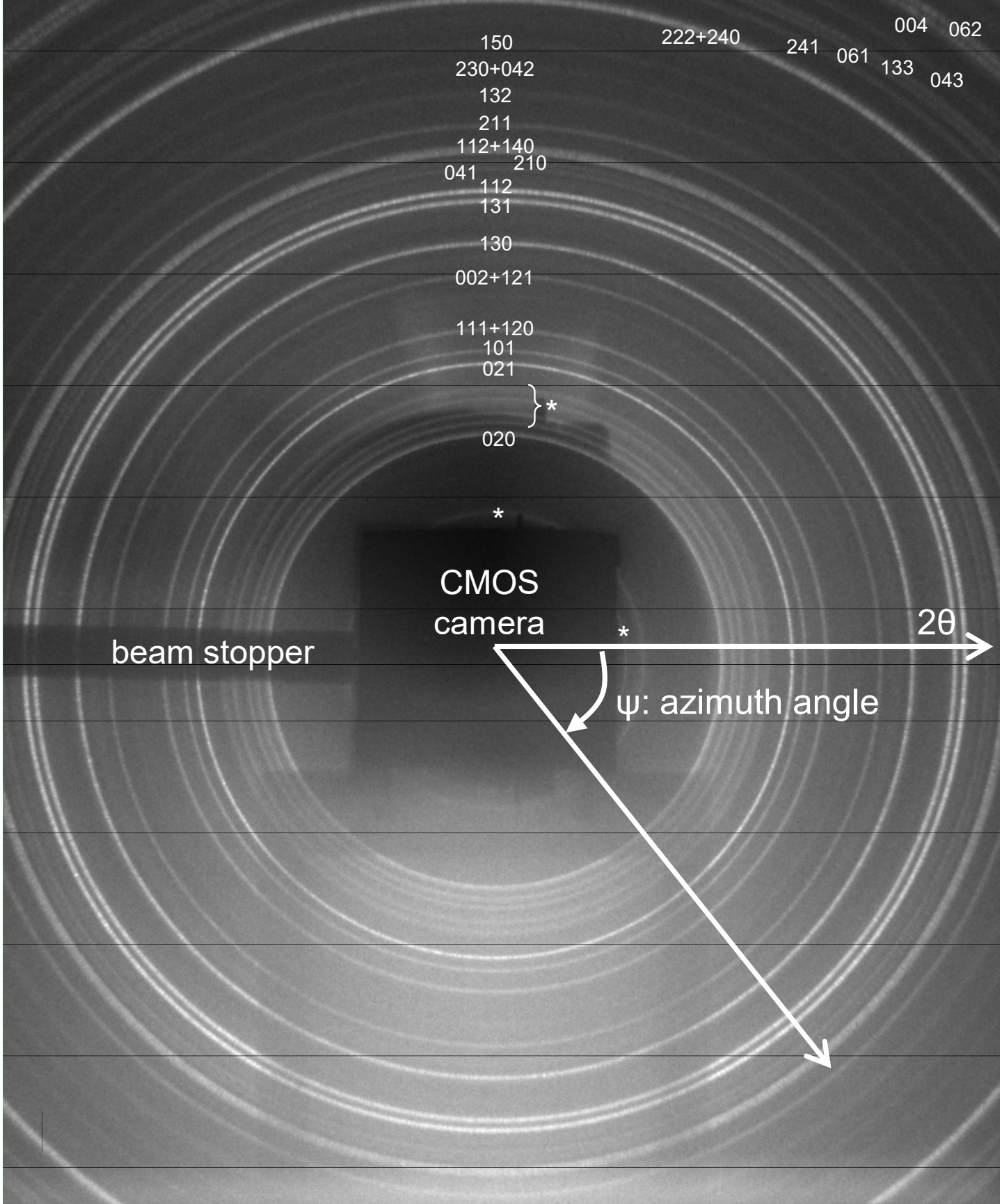
Singh A K, Balasingh C, Mao H K, et al. (1998) Analysis of lattice strains measured under nonhydrostatic pressure. J. Appl. Phys. 83(12):7567–7575. doi: 10.1063/1.367872.

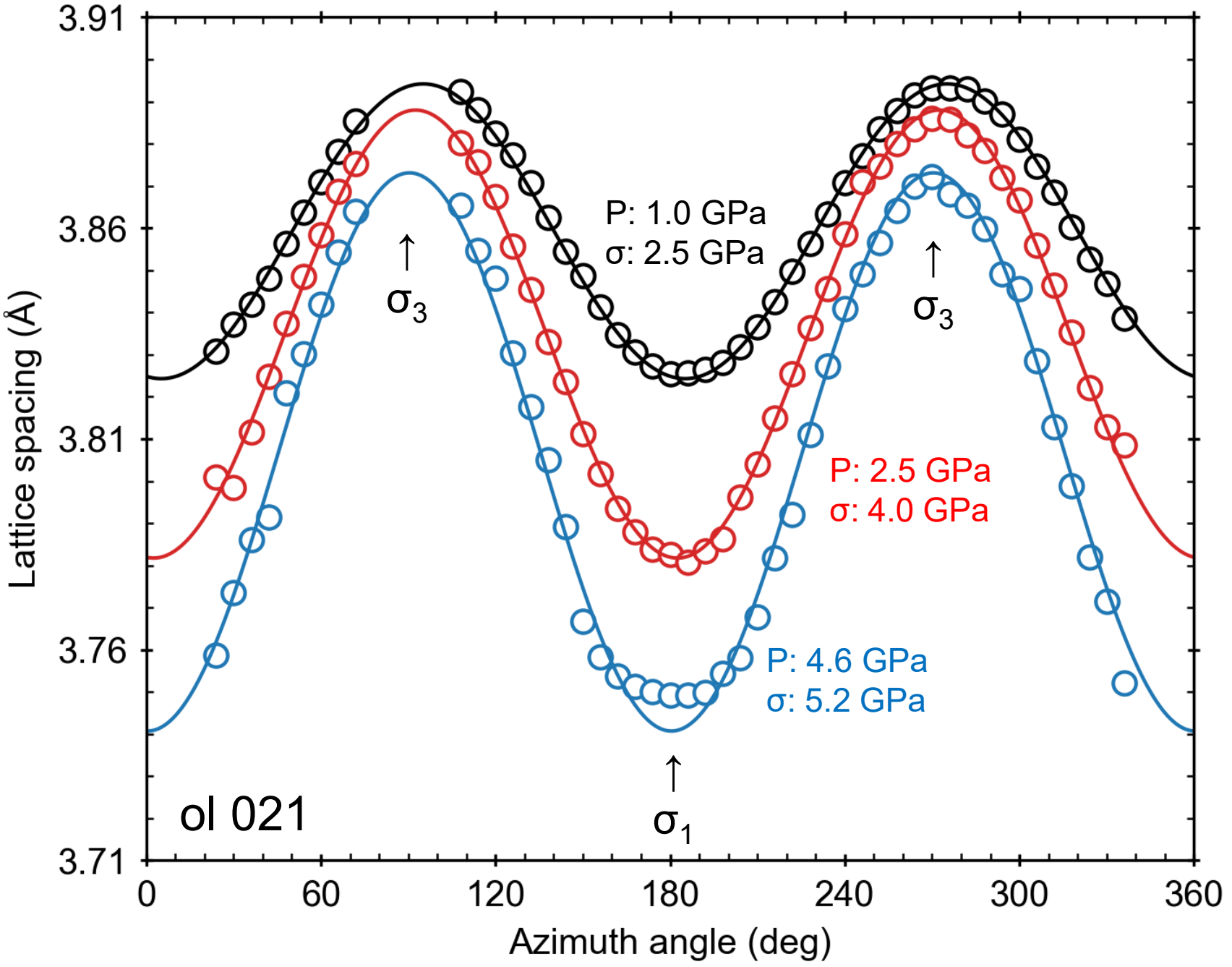
Tsenn M C, Carter N L (1987) Upper limits of power law creep of rocks. Tectonophysics.136:1–26. doi: 10.1016/0040-1951(87)90332-5.

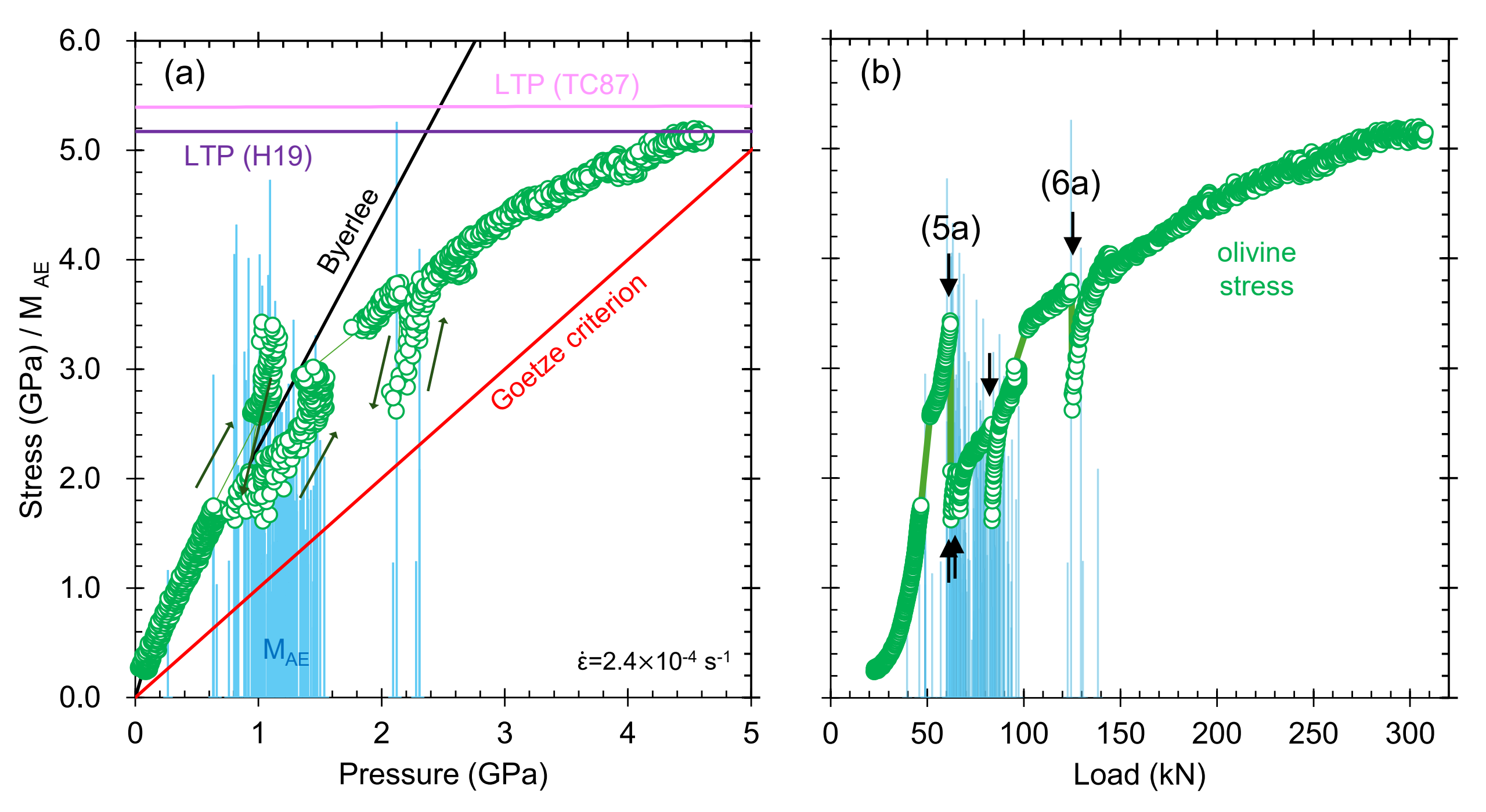
Wiebols G, Cook N (1968) An energy criterion for the strength of rock in polyaxial compression. Int. J. Rock Mech. Min. Sci. 5:529–49. doi: 10.1016/0148-9062(68)90040-5.

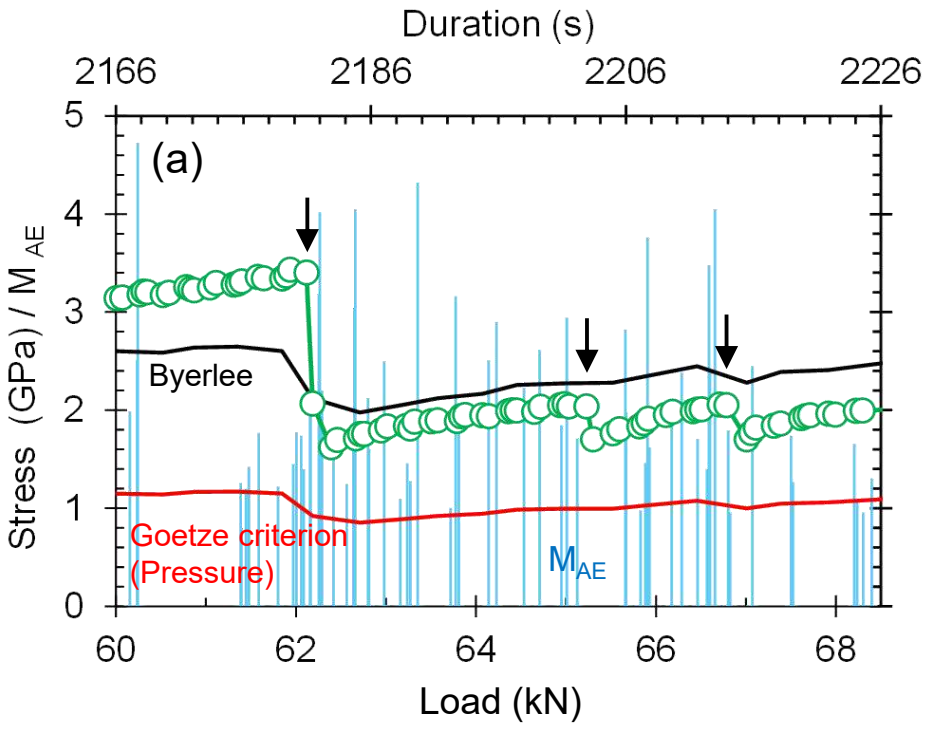
Yumoto H, Koyama T, Yamazaki H, et al. (2025) An X-ray beamline for utilizing intense, high-energy undulator radiation. J. Synchrotron Radiat. 32(5):1201–1210. doi: 10.1107/S1600577525006903.

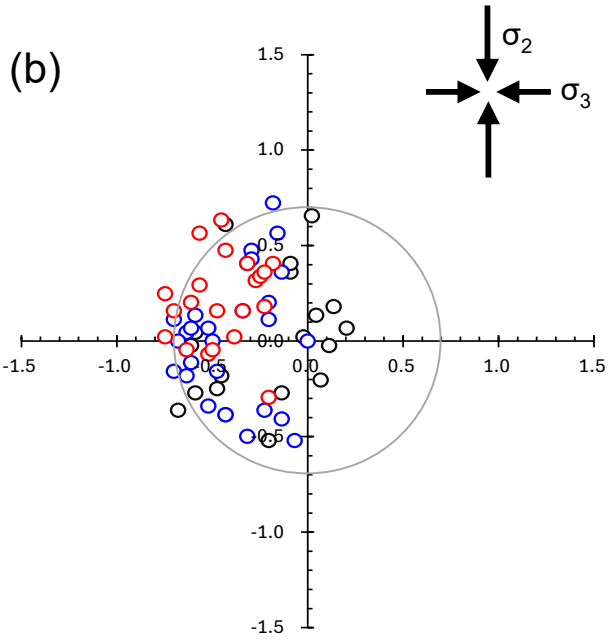

(a)
Cu
Porous Al_2O_3
σ_1
σ_3
Sample
(Forsterite)
Dense Al_2O_3
Pressure
medium
1mm
(b)
1mm
Boron+epoxy
σ_2
σ_3
NaCl
Fo
X-ray

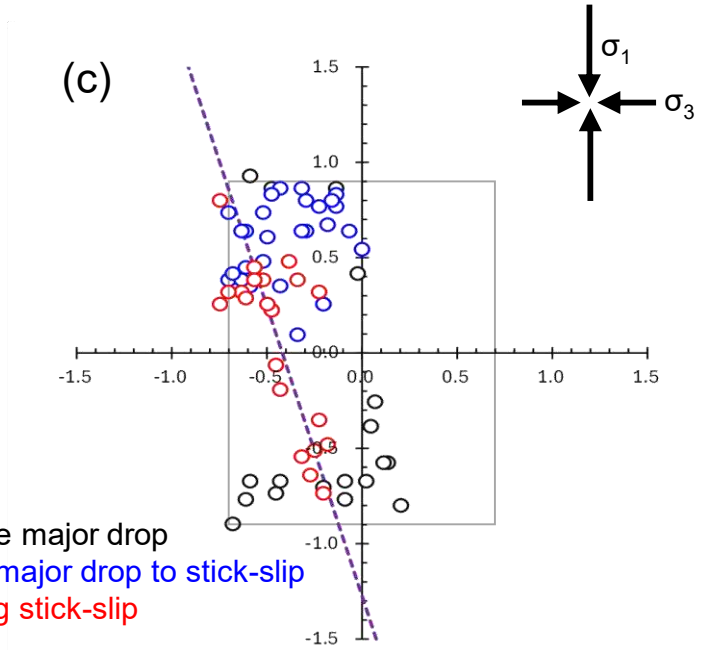

004
062
150
222+240
241
061
133
230+042
043
132
211
112+140
210
041
112
131
130
002+121
111+120
101
021
*
020
*
CMOS
camera
*
2θ
beam stopper
ψ: azimuth angle

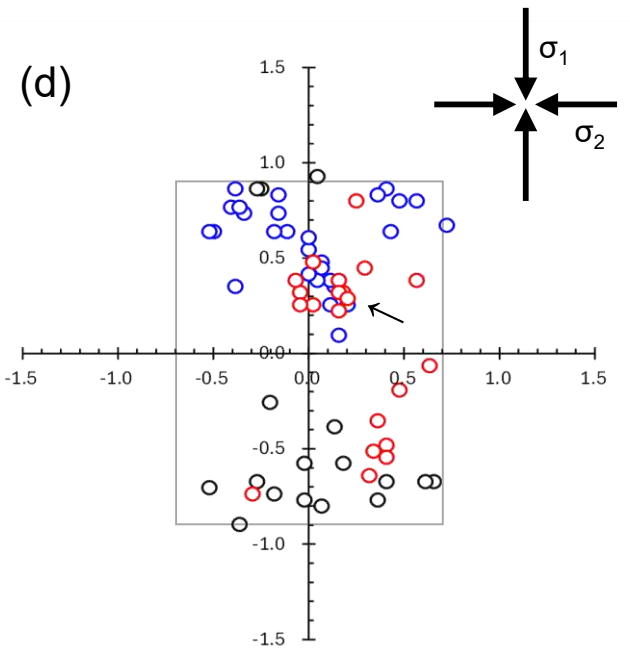

3.91
3.86
3.81
3.76
3.71
Lattice spacing (Å)
0
60
120
180
240
300
360
Azimuth angle (deg)
P: 1.0 GPa
σ: 2.5 GPa
P: 2.5 GPa
σ: 4.0 GPa
P: 4.6 GPa
σ: 5.2 GPa
σ3
σ3
σ1
ol 021

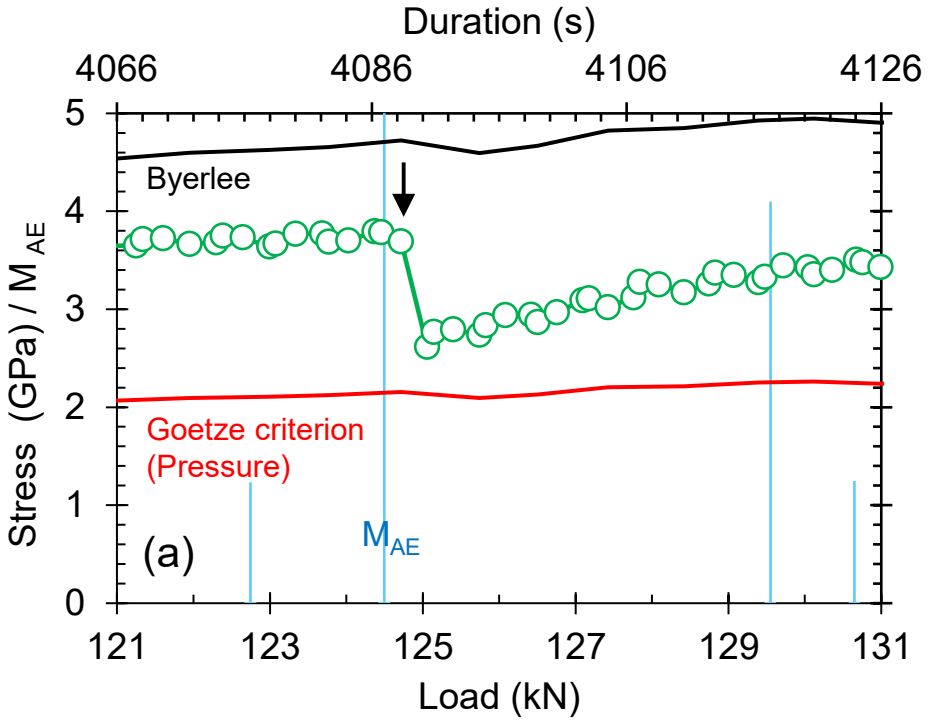

(a)
LTP (TC87)
LTP (H19)
Byerlee
Goetze criterion
M_{AE}
$\dot{\varepsilon}=2.4\times10^{-4}$ s^{-1}
Stress (GPa) / M_{AE}
Pressure (GPa)
0.0
1.0
2.0
3.0
4.0
5.0
6.0
0
1
2
3
4
5
(b)
(5a)
(6a)
olivine stress
Load (kN)
0
50
100
150
200
250
300

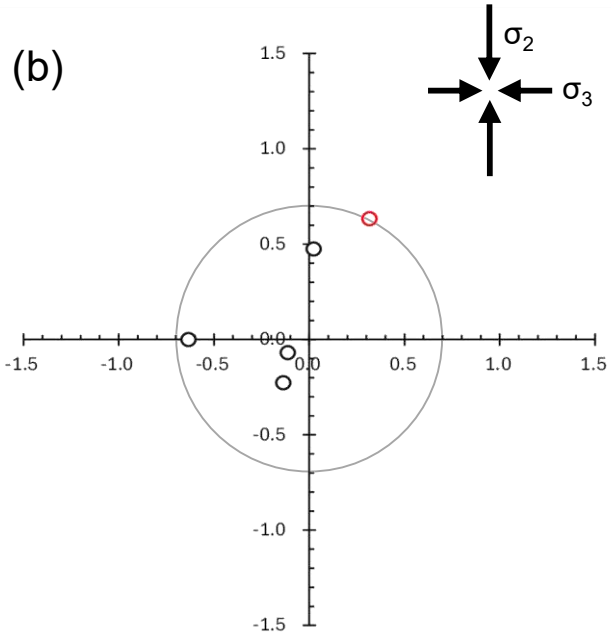

Duration (s)
2166
2186
2206
2226
(a)
Stress (GPa) / M AE
Byerlee
Goetze criterion
(Pressure)
M AE
Load (kN)
60
62
64
66
68

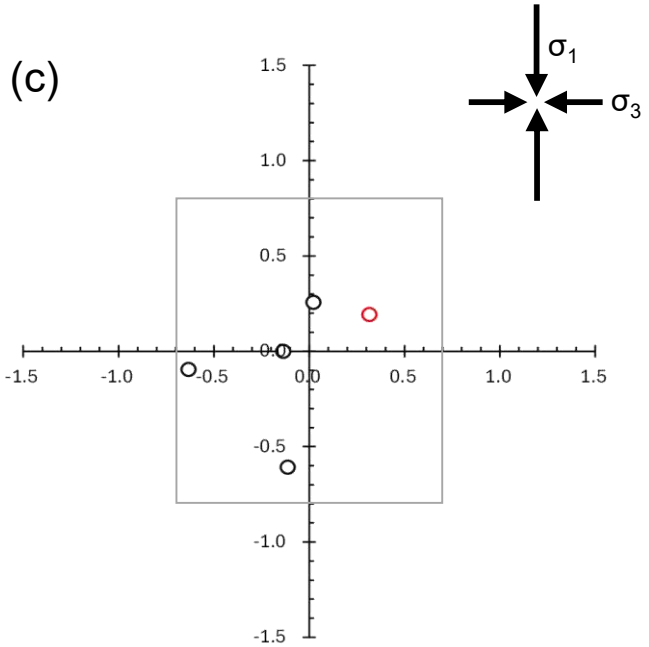

(b)
σ2
σ3

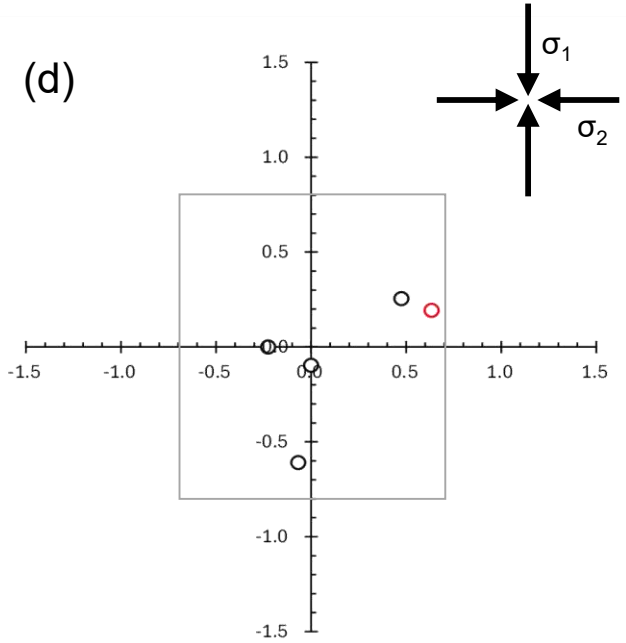

(c)
σ1
σ3
○: before major drop
○: from major drop to stick-slip
○: during stick-slip

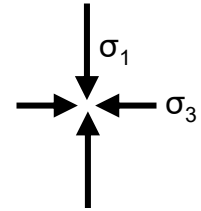

(d)
σ1
σ2


Duration (s)
4066
4086
4106
4126
Byerlee
Goetze criterion
(Pressure)
(a)
M_{AE}
Stress (GPa) / M_{AE}
Load (kN)
121
123
125
127
129
131


(b)
σ_2
σ_3


(c)
σ_1
σ_3


(d)
σ_1
σ_2



(a)

z \ y	-2.38	-2.18	-1.98	-1.78	-1.58	-1.38	-1.18
-2.30	2.8	3.1	1.6	1.9	2.3	2.9	2.9
-2.50	2.8	2.9	3.1	2.4	3.0	3.3	2.9
-2.70	2.8	2.8	3.1	2.7	3.1	3.2	2.7
-2.90	2.7	2.8	3.3	3.1	3.1	2.8	2.5
-3.10	3.1	2.8	2.9	3.3	2.9	2.7	2.3
-3.30	2.8	2.8	3.1	3.5	3.4	2.7	2.3
-3.50	3.1	2.7	3.1	3.2	3.2	2.7	2.6
-3.70	3.0	3.1	3.0	2.6	2.8	2.7	2.3
-3.90		2.5	2.8	2.5	2.8	2.5	2.0

(b)

z \ y	-2.70	-2.50	-2.30	-2.10	-1.90	-1.70	-1.50
-2.15		4.2	3.4	2.5	2.8	3.1	2.9
-2.35		3.8	4.1	3.3	3.7	3.9	3.6
-2.55	3.5	3.9	4.0	3.9	4.1	4.0	3.2
-2.75	3.3	3.5	4.0	4.0	4.3	3.8	2.9
-2.95	3.4	3.5	3.9	4.0	4.2	3.7	2.9
-3.15	3.3	3.5	3.6	4.1	4.2	3.8	3.6
-3.35	3.3	3.6	3.5	4.0	3.9	4.0	3.6
-3.55		3.6	3.4	3.4	3.4	3.7	3.5
-3.75							

(c)

z \ y	-2.50	-2.30	-2.10	-1.90	-1.70	-1.50
-2.00		4.6	3.9	4.0	4.1	3.9
-2.20		5.2	4.8	4.7	4.8	4.6
-2.40	5.1	4.9	5.1	5.0	5.1	4.6
-2.60	4.8	4.8	5.0	5.2	5.4	4.6
-2.80	4.6	4.7	4.9	5.1	5.3	4.7
-3.00		4.9	4.8	4.8	5.1	4.9
-3.20		4.8	4.8	4.8	5.1	4.9
-3.40			4.4	4.2	4.3	
-3.60						

Stress: 1.0 GPa 5.4 GPa

Supplementary Files

This is a list of supplementary files associated with this preprint. Click to download.

- GraphicalAbstract.png
- SupplementaryFigure.pdf